Ceramics International 45 (2019) 15244–15251

Contents lists available at ScienceDirect

Ceramics International

journal homepage: www.elsevier.com/locate/ceramint

Influence of defects on photoluminescent and photocatalytic behavior of $CaO/SrTiO_3$ heterojunctions

Ubirajara Coleto Jr.[a,b,*], Rafael A.C. Amoresi[c], Chrystopher A.M. Pereira[a], Alexandre Z. Simões[c], Maria A. Zaghete[a], Elias S. Monteiro Filho[a], Elson Longo[d], Leinig A. Perazolli[a]

[a] LIEC – Chemistry Institute, São Paulo State University – UNESP, 14800-060, Araraquara, SP, Brazil
[b] Department of Chemistry – Federal Institute of São Paulo – IFSP, 15808-305, Catanduva, SP, Brazil
[c] Faculty of Engineering of Guaratingueta - UNESP, 12516-410, Guaratinguetá, SP, Brazil
[d] LIEC - Department of Chemistry, São Carlos Federal University - UFSCar, 13565-905, São Carlos, SP, Brazil

ARTICLE INFO

Keywords:
A. powders: chemical preparation
B. Nanocomposites
B. Defects
Photocatalyst

ABSTRACT

$CaO/SrTiO_3$ heterostructures were fabricated, and their photocatalytic activity for the discoloration of Rhodamine B (RhB) dye was evaluated. $SrTiO_3$ particles were obtained via a polymer precursor method, and heterojunctions in which CaO grew on $SrTiO_3$ crystalline particles were prepared via a sol-gel route. Characterization was performed using X-ray diffraction, transmission electron microscopy, and ultraviolet/visible/near-infrared, Raman, and photoluminescence spectroscopy. The photocatalytic activity of the heterostructures was verified by the discoloration of RhB using UV light. Defects caused by tensile strain in the interface region were verified when the calcium oxide grew on the strontium titanate, altering the defects of the material. In the heterojunctions, the defects of the monoionized and doubly ionized O (oxygen) vacancies had a greater contribution to the photocatalytic process than the defects at deep levels generated in the stress region and the direct transfer of charge between the conduction and valence bands.

1. Introduction

Pure CaO has been studied as a photocatalyst material [1–3]. Additionally, CaO doped with metal ions and CaO in heterostructure form, e.g., with TiO_2 oxide [4–7], have been investigated. During the synthesis of CaO, other phases, such as hydroxide ($Ca(OH)_2$) and carbonate ($CaCO_3$), can be detected, which also exhibit significant photocatalytic activity [1,3]. These materials have been evaluated in several processes, such as dye discoloration [1–3], biodiesel production via transesterification of palm oil [7], esterification of free fatty acids [4,6], synthesis of organic compounds [4], and degradation of drugs [5] and ammonia [8]. The photocatalytic activity using ultraviolet (UV) light [1–4,7], sunlight [5,8], and with different wavelengths ranging from UV to near-infrared (NIR) [6], has been studied.

Mixtures of CaO and TiO_2 were used in [7] to obtain biodiesel via photocatalysis, resulting in > 96% conversion of oil into biodiesel. Abbas et al. (2017) used a heterogeneous CaO/TiO_2 catalyst to synthesize a wide variety of biologically active molecules, i.e., vitamin B6 analogues, with a yield of > 90%, and biodiesel from free fatty acids, with a yield of 97%. Different phases of Ca - hydroxide, hydrated lime, oxide, and carbonate - were evaluated as photocatalysts for the degradation of Rhodamine 6G. $Ca(OH)_2$ is the most photoactive phase, with a bandgap of 5.69 eV. It behaves as an insulating material, and its photocatalytic activity is attributed to the indirect sensitization of the dye. The photoactivity is related to electron transfer from the dye to the insulation material; that is, under irradiation, the dye is excited and injects electrons into the conduction band (CB), which interact with the adsorbed species on the surface of $Ca(OH)_2$, producing radical species for the degradation of the dye [1].

$SrTiO_3$ is an oxide perovskite in which Sr^{2+} occupies the vertices of the octahedral cluster of $[TiO_6]$ of a cubic crystalline system [9]. This oxide is an n-type semiconductor with a bandgap energy of approximately 3.2 eV [10]. For this perovskite, the valence band (VB) is predominantly composed of O 2p orbitals, with a small contribution of Ti 3d orbitals, and the CB is composed mainly of 3d Ti orbitals and 3d Sr orbitals at high energies [11]. The photocatalytic activity of the Ti and Sr sites at the surface of the $SrTiO_3$ structure for reducing CO_2 was studied, and the results indicated that the chemical environment surrounding the Ti^{4+} ions was propitious to the photoactivity and that $SrTiO_3$ promoted the electronic transitions [12].

Heterojunctions composed of $BiFeO_3/TiO_2$, $SrTiO_3/TiO_2$, $PbTiO_3/TiO_2$, MoS_2/TiO_2 and NiO/TiO_2 have been used in several applications,

* Corresponding author. LIEC – Chemistry Institute, São Paulo State University – UNESP, 14800-060, Araraquara, SP, Brazil.
E-mail address: biracoleto@ifsp.edu.br (U. Coleto).

https://doi.org/10.1016/j.ceramint.2019.05.013
Received 20 March 2019; Received in revised form 2 May 2019; Accepted 2 May 2019
Available online 06 May 2019

such as fuel cells, sensors, catalysts, magnetic materials, and corrosion protection [13–15]. Heterojunction materials are promising as photocatalysts owing to the generation of structural defects at the interface, which increases the recombination time of the photogenerated electrons/holes and thus increases the photocatalytic activity [16–21]. In this study, we fabricated CaO/$SrTiO_3$ heterojunctions via a simple sol-gel method. The heterojunctions had dissimilar mechanisms of charge transfer between different types of defects, yielding unusual photocatalytic activities. The desired defects were obtained by changing the $SrTiO_3$ concentration.

2. Experimental

The CaO and $SrTiO_3$ used in this work were prepared via a polymeric precursor method, and the CaO/$SrTiO_3$ heterostructures in which CaO grew on $SrTiO_3$ crystalline particles were prepared via a sol-gel route.

CaO was obtained by mixing 1.0 mol of calcium nitrate tetrahydrate (99.0%–103.0%, Synth) with 4.0 mol of citric acid (99.8%, ECIBRA) and 16.0 mol of ethylene glycol (99.9%, Neon). The Ca salt was dissolved in approximately 100 mL of deionized H_2O, and then citric acid and ethylene glycol were added. The solution was stirred for 2.5 h at a temperature of 130 °C until the liquid became a nearly solid gel. The formed product was heated in a muffle oven at 250 °C/1 h with a continuous air flow, and then the temperature was increased to 350 °C/4 h. The generated solid was triturated in a mortar and subjected to further heat treatment with a continuous air flow at 350 °C/12 h. Finally, it was subjected to heat treatment in a muffle furnace at 1000 °C/4 hunder a continuous air flow. $SrTiO_3$ particles were prepared via a route similar to that for CaO, with titanium isopropoxide (97%, Sigma-Aldrich) and strontium acetate (Sigma-Aldrich) as precursors. The ratio of metal, citric acid, and ethylene glycol was maintained. The mixture was stirred at a temperature of 120 °C/9 h. Heat treatment was performed at 350 °C/4 h, and the generated solid was triturated and subjected to further heat treatment at 600 °C/4 h.

The heterostructure was preparedusing a sol-gel route. The first step involved the hydroxylation of the surface of the $SrTiO_3$ particles via the addition of H_2O_2 (20%–60%, Vetec), NH_4OH (28%–30%, Qhemis), and deionized water under heat treatment at 50 °C/30 min. Then, drops of acrylic acid (99%, Sigma–Aldrich), 2-methoxyethanol (99.8%, Sigma-Aldrich), and polyvinyl alcohol (99.6%, Vetec) were added for 30 min at 50 °C with stirring, yielding a stable $SrTiO_3$ suspension. In the second step, calcium nitrate tetrahydrate (99.0%–103.0%, Synth) was dissolved in isopropyl alcohol (99.5%, Vetec), forming a solution of Ca. Then, the $SrTiO_3$ stable suspension was added to the Ca solution. The resulting mixture was stirred at 150 °C/1 h to promote the coating of the $SrTiO_3$ particles with CaO. The generated solid was heated in a muffle oven, with air injection, at 150 °C/12 h to eliminate the organic matter. Then, further heat treatment was performed at 600 °C/4 h. The sample was only inserted in the oven when the temperature was already at 600 °C, with air injection, avoiding the temperature range of 400–600 °C, which is critical for the formation of the $CaCO_3$ phase. The resulting heterojunctions were denoted as Ca + 0.5%STO, Ca + 1%STO, Ca + 2%STO, Ca + 5%STO, and Ca + 10%STO, corresponding to 0.5%, 1%, 2%, 5%, and 10% $SrTiO_3$ particles (by mass) added to the sol-gel solution of Ca, respectively.

The heterojunctions were characterized via X-ray diffraction (XRD) analysis using a diffractometer (RINT2000, Rigaku®), via UV/visible (vis)/NIR absorption spectroscopy in the diffuse-reflectance mode in the spectral range of 200–800 nm using a spectrophotometer (LAMBDA 1050, PerkinElmer®), and via photoluminescence spectroscopy using a 325-nm-wavelength excitation laser, where the exciton recombination was measured from 350 to 850 nm and the generated spectra were deconvoluted by employing the Peak Fit® software. The generated spectra via Raman were obtained using a Horiba Jobin Yvon® LabRAM HR spectrometer and high-resolution transmission electron microscopy (HRTEM) using FEI TECNAI G^2 F20 HRTEM® equipment.

To evaluate the photoactivity of the heterojunctions, photocatalysis was performed using UV light (λ_{max} = 254 nm, 11 W, Osram, Puritec HNS 2G7) under constant stirring and air bubbling. For the photocatalytic experiments, 700 mL of an aqueous solution of 1×10^{-5} mol/L of Rhodamine B (RhB) was used, which was sonicated for 20 min in a dark room. During the catalytic process, an aliquot was removed before the suspension was sonicated, and approximately 20 min after the sonication, another aliquot was removed (time zero). Subsequently, aliquots were removed 5, 10, 15, 30, 60, 90, and 120 min after the beginning of the photocatalysis process. The aliquots were centrifuged and analyzed using a spectrophotometer (80 PR, Femto Cirrus®) at 554 nm. The photocatalytic efficiency was calculated according to the percentage of the absorbance of the RhB solution, by using Equation (1). The half-life ($t_{1/2}$) of the RhB photo-discoloration was calculated using Equation (2).

$$A\% = \frac{C_0 - C_t}{C_0} \cdot 100 \quad (1)$$

$$t_{1/2} = \frac{\ln 2}{k} \quad (2)$$

3. Results and discussion

3.1. Photoactivity of catalysts for discoloration of RhB

Fig. 1a shows a graph of the photolysis and photocatalysis with respect to time for the pure materials CaO and $SrTiO_3$, as well as the CaO/$SrTiO_3$ heterostructures (0.5%, 1%, 2%, 5%, and 10% m/m of $SrTiO_3$), for the discoloration of RhB using UV light. The discoloration of RhB via photocatalysis had pseudo-first-order kinetics. The results for ln (A_0/A) with respect to time, as shown in Fig. 1b, were used to calculate the kinetic parameters of the dye discoloration for the systems studied. The results are presented in Table 1.

Table 1 shows the kinetic parameters of the RhB photo-discoloration: the percentage of discoloration after 120 min of reaction, the reaction rate constant, the calculated half-life ($t_{1/2}$), and the observed half-life ($t_{1/2}$).

The results indicate that the heterostructures exhibited better photo-discoloration performance than the pure CaO and $SrTiO_3$. The heterostructures composed of 0.5% and 2% $SrTiO_3$ (relative to CaO) were the most efficient for the dye discoloration, reaching 92.5% for $t_{1/2}$ = 30 min (Ca + 2%STO). As the content of the $SrTiO_3$ phase in the heterostructures increased beyond 2%, a gradual decrease in the photocatalytic activity was observed. To investigate the differences in the photocatalytic behavior due to the phase composition, XRD, TEM, and photoluminescence measurements were performed.

3.2. Microstructural characterization

The crystalline phases present in the $SrTiO_3$ and CaO samples and the CaO/$SrTiO_3$ heterostructures were analyzed via XRD and transmission electron microscopy (TEM), as shown in Fig. 2a and b, respectively.

As shown in Fig. 2a, the XRD patterns of CaO and $SrTiO_3$ were compared to the JCPDS standards for CaO (ICSD: 51409) and $SrTiO_3$ (ICSD: 23076), respectively. The CaO exhibited peaks at 32.2°, 37.3°, 53.8°, 64.1°, 67.3°, and 79.6°, which were related to the (111), (200), (220), (311), (222), and (400) planes, respectively, of the CaO cubic phase (space group Fm-3m). It also exhibited peaks at 18.0°, 28.7°, 34.1°, 47.1°, 50.8°, 54.4°, 62.6°, and 71.8°, corresponding to the (001), (100), (101), (102), (110), (111), (021), and (022) planes, respectively, of the $Ca(OH)_2$ phase (ICSD: 73467). The $SrTiO_3$ exhibited peaks at 22.7°, 32.4°, 40.0°, 46.4°, 52.3°, 57.8°, 67.8°, and 72.5°, corresponding to the (100), (110), (111), (200), (210), (211), (220), and (221) planes,

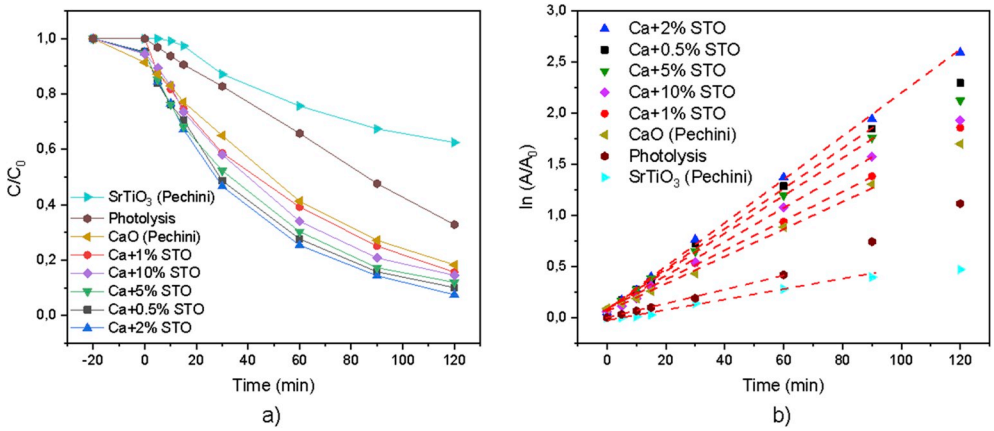

Fig. 1. a) Photocatalytic activity of CaO, $SrTiO_3$, and CaO/$SrTiO_3$ heterostructures and photolysis in the discoloration of RhB using UV light; **b)** ln (A_0/A_t) versus time for discoloration.

Table 1
Kinetic parameters of photolysis and photocatalysis for CaO, $SrTiO_3$, and CaO/$SrTiO_3$ in the discoloration of RhB.

Sample	Discoloration (120 min) (%)	k_{app} x 10^{-2} (min^{-1})	$t_{1/2}$ – calculated (min)	$t_{1/2}$ - observed (min)
Photolysis	67.2	0.806	86.2	85.7
$SrTiO_3$ (Pechini)	37.5	0.423	163.8	–
CaO (Pechini)	81.7	1.356	51.1	48.8
Ca + 0.5%STO	91.4	1.864	37.2	38.8
Ca + 1%STO	84.4	1.525	45.5	43.3
Ca + 2%STO	92.5	2.377	29.2	27.5
Ca + 5%STO	88.0	1.979	35.0	33.1
Ca + 10%STO	85.5	1.729	40.1	40.0

respectively, of the cubic crystalline phase of $SrTiO_3$ (space group Pm-3m). For the CaO/$SrTiO_3$ heterostructures, the most intense XRD peak for $SrTiO_3$ (at 32.4°, corresponding to the (110) plane) overlaps with the peak at 32.2° (corresponding to the (111) plane) for CaO. The low-intensity peak observed at 29.5° is attributed to the formation of $CaCO_3$ (ICSD: 18164), which is typical for CaO samples. The peak intensities in the heterostructure patterns (e.g., at 32°) are higher than those in the CaO patterns. This increase is attributed to the presence of $SrTiO_3$. The heterostructure composed of Ca + 10%STO exhibited a peak at approximately 46.5°, corresponding to the (200) plane of $SrTiO_3$. This sample showed low-intensity peaks at 18.1° and 34.1°, corresponding to the (001) and (101) planes, respectively, of the $Ca(OH)_2$ phase. The heterostructures exhibited similar XRD profile sowing to the phases of their precursors.

As shown in Fig. 2b, HRTEM was performed on the samples to observe the interface region between the CaO and $SrTiO_3$ phases and determine the interplanar distance of the crystalline planes. An interplanar distance of 2.76 Å, which is attributed to the (110) plane of the $SrTiO_3$, is observed in the image. Around this region, there are interplanar distances of 1.70 and 2.40 Å, corresponding to the (220) and (200) planes, respectively, of the CaO phase. These results indicate the formation of the heterostructure between the cubic structures of CaO (a = 4.81059 Å) and $SrTiO_3$ (a = 3.90500 Å).

Raman scattering spectroscopy indicated that the main modes were related to $CaCO_3$ and $Ca(OH)_2$ for all the samples, as shown in Fig. 3. This is evident because Raman active modes corresponding to the cubic structure of CaO were not observed, except for second-order scattering by phonons. Therefore, the modes observed in the spectra were mainly composed of calcium hydroxide and calcium carbonate. As the $SrTiO_3$ concentration in the heterostructures increased to 5%, the mode located at 282 cm^{-1} for the 0.5% sample shifted to 279 cm^{-1}. Along with this

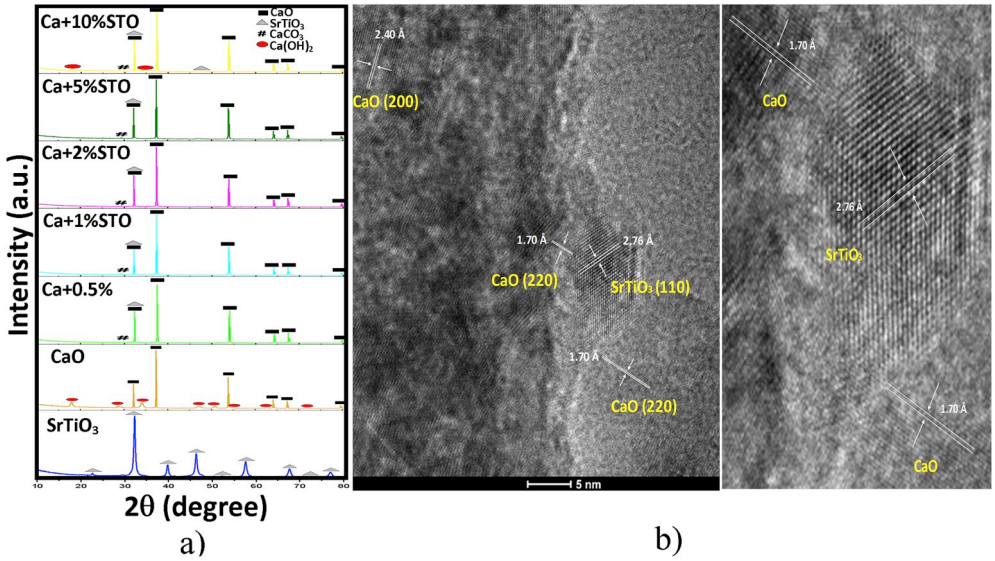

Fig. 2. a) XRD patterns of CaO, $SrTiO_3$, and the heterostructures: Ca + 0.5%STO, Ca + 1%STO, Ca + 2%STO, Ca + 5%STO, and Ca + 10%STO. **b)** HRTEM image of the Ca + 10%STO heterostructure. A magnified view of the central region is shown on the right.

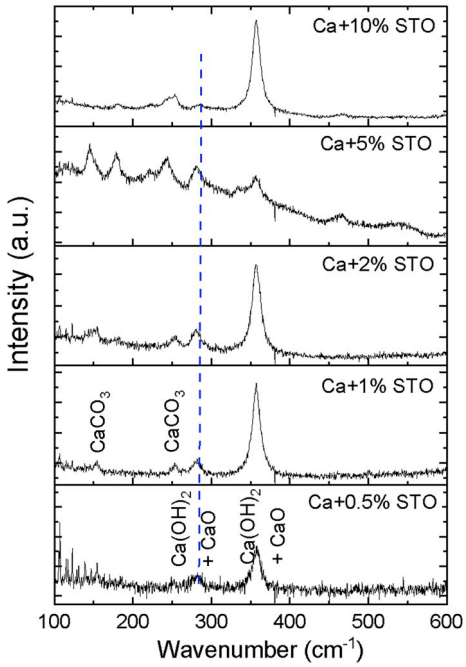

Fig. 3. Raman spectra of the heterostructure samples.

shift, the suppression of the most intense modes (~360 cm^{-1}) and the appearance of modes at 179 and 333 cm^{-1} were observed. Factors such as phonon confinement, defects, non-stoichiometry, and crystal lattice stress contributed to the observed behavior [22,23]. In the case of heterojunctions, it is expected that stress - such as tension or compression of the crystalline lattice - is induced in the interface region between the structures, forming defects [15]. Defects, e.g., those due to tensile strain of the crystal lattice, cause the Raman modes to redshift [24–26]. In our results, this redshift was evident and was due to defects caused by the tensile strain in the interface region when the CaO (a = 4.81059 Å) grew on the crystalline particles of $SrTiO_3$ (a = 3.90500 Å). The suppression of the mode intensity and the formation of new modes in the 5% sample were related to the local symmetry breaking in the interface region. This symmetry breaking restricted and diminished the typical vibrational modes of the structure, while creating new points of short-range symmetry represented by the formation of the new modes. The spectrum of the sample with 10% $SrTiO_3$ resembled that of the sample with 0.5% $SrTiO_3$, and there was probably no interaction between the phases, as for the samples with up to 5% $SrTiO_3$. Therefore, the short-range analysis allowed the tensile strain intensity to be investigated as a function of the $SrTiO_3$ concentration in the heterostructure.

3.3. Optical characterization

Fig. 4 illustrates the photoluminescence behavior of CaO, Ca + 0.5% STO, Ca + 1%STO, Ca + 2%STO, Ca + 5%STO, Ca + 10%STO, and $SrTiO_3$ samples. For the analysis, the excitation wavelength was 325 nm, and the emission range was 350–850 nm. The spectra of the samples showed that the recombination of the excitons (pairs consisting of an electron in an excited state and a hole) occurred at different energy levels, from 3.45 eV (360 nm) to approximately 1.46 eV (850 nm). The energy range from the UV region (360 nm) to the red region (700 nm) exhibited the highest luminescence emission, as indicated by the broadband of the spectrum.

To elucidate the photoluminescent behavior, the spectra were deconvoluted, as shown in Fig. 5. Each component represents a radiative decay, corresponding to the relaxation of the electrons from a higher energy level to a lower energy level, and the sum of all the radiative

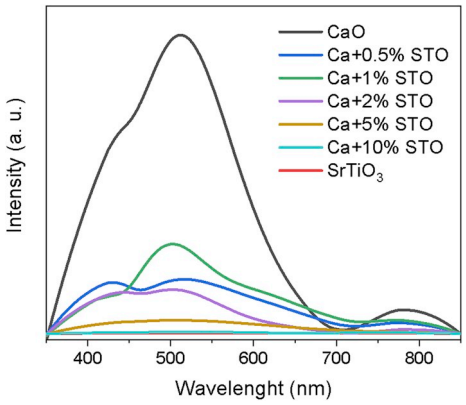

Fig. 4. Photoluminescence spectra of CaO, $SrTiO_3$, and the heterojunctions at room temperature.

processes resulted in the broadband. The defects located at electronic levels near the VB and CB were classified as shallow and formed bands in the high-energy region (blue). Defects located at electronic levels near the Fermi level were classified as deep defects and correspond to photoluminescent emissions in regions of lower energy (green/yellow/red) [27–29]. Emissions in the violet region represent the band–band radioactive decay due to the recombination of the electron-hole pairs [27,30], whereas the blue emissions indicate the presence of monoionized O vacancies [20,31,32]. The emissions observed in regions of lower energy (green/yellow/red) are related to doubly ionized O vacancies [16,31]. The spectrum of $SrTiO_3$ (Eg = 3.18 eV, Fig. 6 and Table 2) was deconvoluted in three bands, as shown in Fig. 5. The emission centers were located in the violet, green, and red regions, indicating band–band transitions, i.e., direct transitions from the VB to the CB, and defects at deep levels due to the presence of doubly ionized O vacancies. As shown in Fig. 5, CaO (E_g insulation) exhibited photoluminescent bands similar to those of $SrTiO_3$, with the exception of the band in the red region, which was shifted to the infrared region and to a lesser extent. This was due to the photoluminescent emission caused by the interfacial defects generated by the presence of $Ca(OH)_2$, which had a more compact structure than the cubic CaO and emitted at a lower energy. The Ca + 0.5%STO (E_g = 3.08 and 3.73) and Ca + 1%STO (E_g = 3.04 and 3.38) heterostructures, with inflection of two bandgap energies (Table 2) separated by 0.65 and 0.34 eV, respectively, exhibited photoluminescent bands in the violet, green, red, and infrared regions. The infrared band was generated by defects in the interface region between CaO and $SrTiO_3$, which caused compression stress in the junction of the two cubic phases, as indicated by the Raman spectrum. The red band was due to double-ionized O vacancies generated by the CaO–$SrTiO_3$ interface. Increasing the proportion of $SrTiO_3$ (0.5% → 1%) in the heterostructure reduced the emission in the violet region, indicating reduced direct transitions from the CB to the VB and increased structural defects. The increase of the $SrTiO_3$ concentration beyond 2% increased the concentration of defects in the heterostructure, as indicated by the larger bandgap energy inflection (Table 2). In the photoluminescence spectrum for the 2% heterostructure, there was pronounced emission in the blue region (~50% of the spectrum), and approximately 48% of the spectrum emission was in the green region. The first region corresponds to defects due to monoionized O vacancies, and the second region corresponds to defects due to doubly ionized O vacancies. There was low emission in the infrared region. As the concentration of the $SrTiO_3$ phase increased from 2% to 10%, the emission in the blue and green regions, which were related to the monoionized and doubly ionized O vacancies, respectively, decreased. These were the main defects related to the charge transfer in the interface region of the heterostructure. The enhanced emission in the infrared region was caused by the large amount of defects in the crystalline lattice at the CaO/$SrTiO_3$ interface, such as stress-related

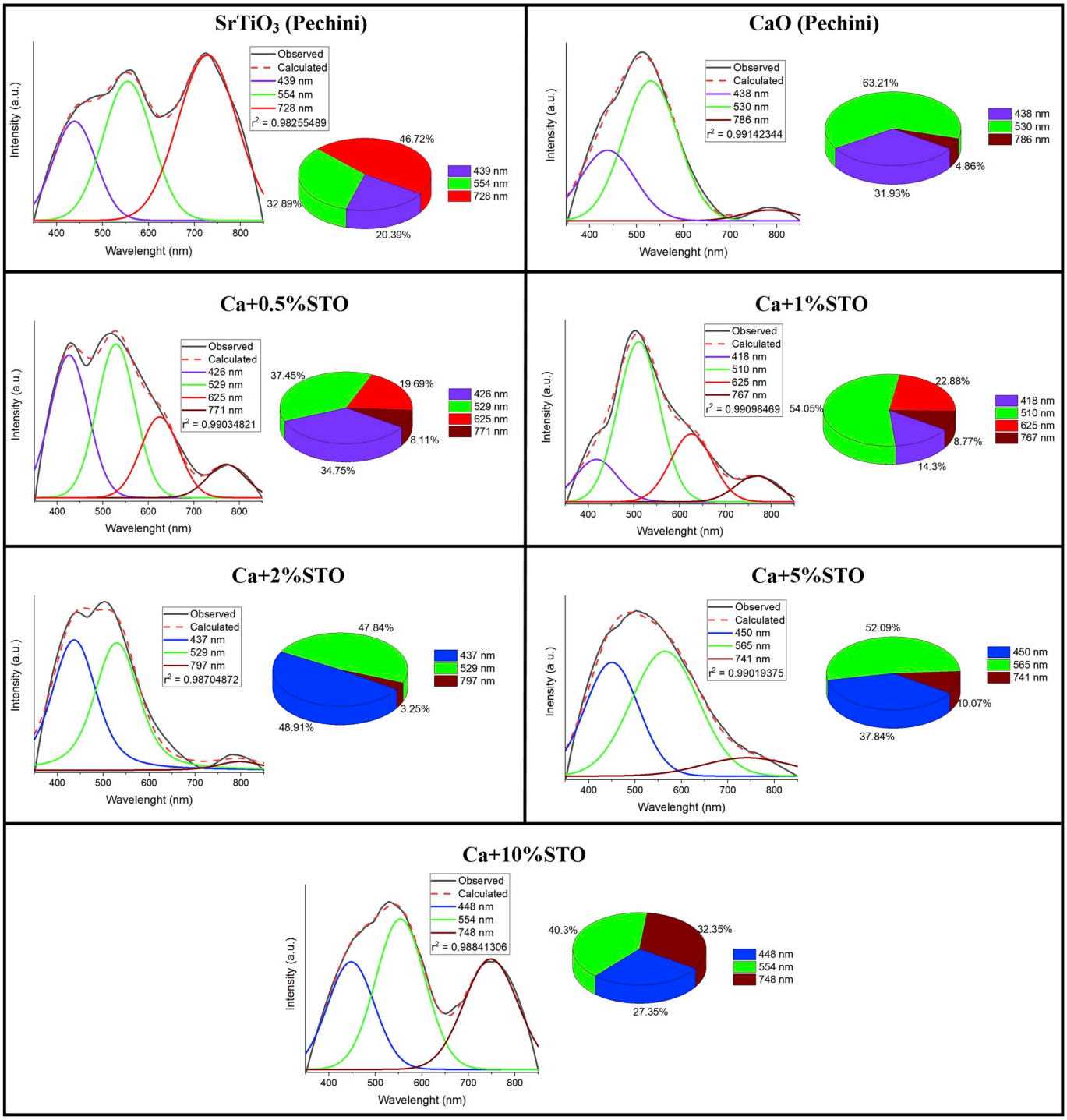

Fig. 5. Deconvolution of the photoluminescence spectra of the $SrTiO_3$, CaO, and $CaO/SrTiO_3$ heterostructure samples.

defects, which resulted in the reduction of the charge transfer between the phases.

The photocatalytic results are related to the defects generated at the interface of the heterostructures, which promoted the charge transfer, generating the species responsible for the oxidation reduction reactions that discolored the RhB. The most photoactive heterostructure - Ca + 2%STO - showed bands in the blue region, indicating monoionized O vacancies; in the green region, indicating doubly ionized O vacancies; and in the infrared region, indicating interfacial defects generated by the formation of the heterostructure. When the concentration of $SrTiO_3$ increased beyond 2%, the amount of interfacial defects increased and the amount of O vacancies decreased, reducing the photoactivity. When the $SrTiO_3$ concentration decreased below 2%, the amount of structural defects decreased and the electrons began to recombine directly from the CB to the VB, as indicated by emission in the violet region. For effective heterostructures, i.e., with easy charge transfer, for the discoloration of RhB, it was verified that the electronic holes and superoxide radicals (generated by the excited electrons) were the most active species [20]. Therefore, the emissions in the blue, green, and red regions were responsible for the increase in photocatalytic activity. In contrast, the emissions in the violet and infrared regions appeared to retard the photocatalytic effect.

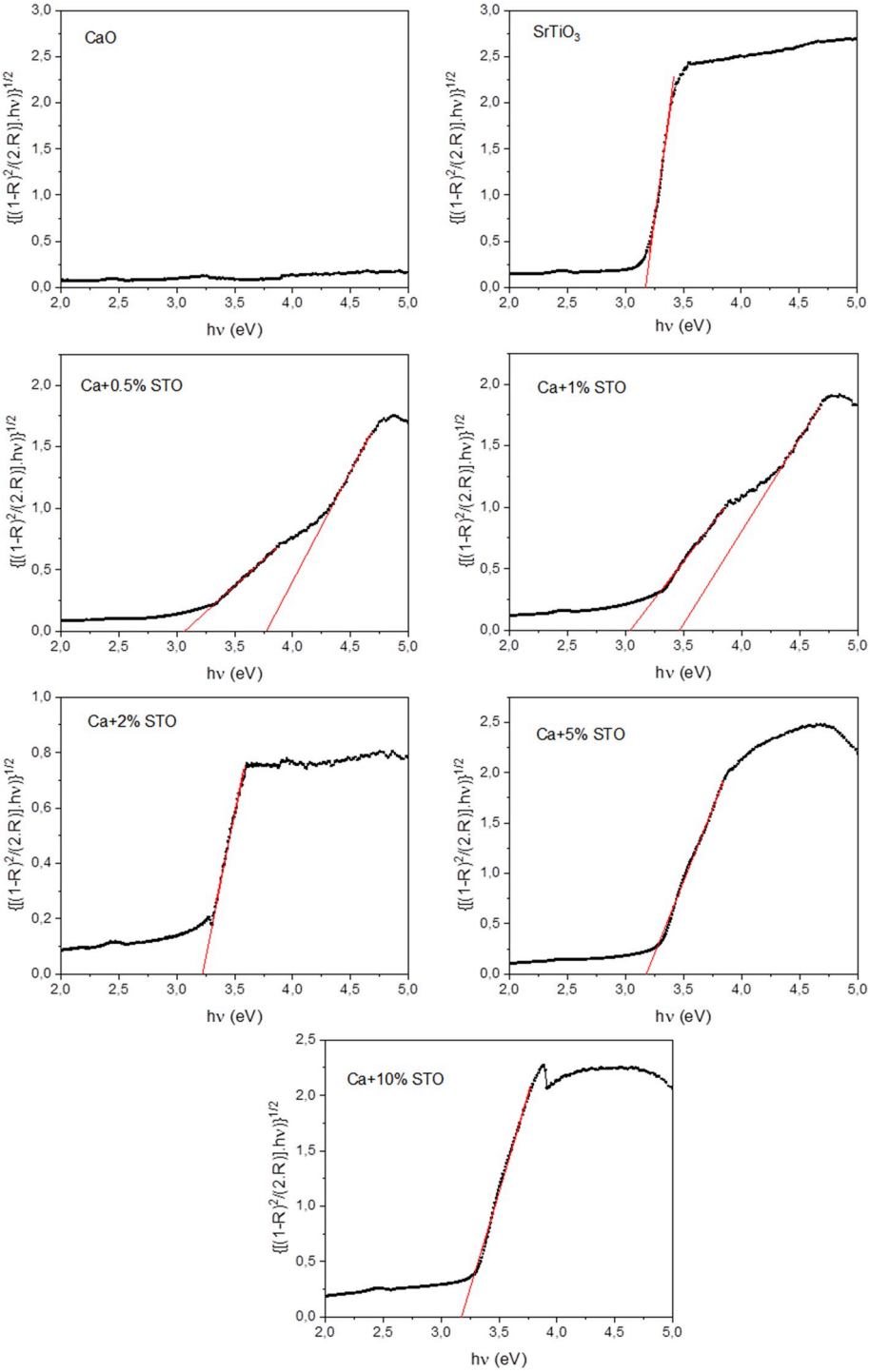

Fig. 6. Tauc plot of CaO, $SrTiO_3$, and CaO/$SrTiO_3$ heterostructure samples.

3.4. Heterojunction charge-transfer model

We propose a photocatalytic model for the semiconductor heterojunction considering that pure CaO behaves as an insulator with photocatalytic activity (81.7% discoloration of RhB). The behavior was determined to be either photocatalytic or only catalytic. Tests were performed under the aforementioned conditions, but in the absence of light. In Fig. 7, the results are illustrated and compared with those obtained under light.

The percentage of RhB dye discoloration with respect to time for CaO particles in the presence of light and in the dark are shown in Fig. 7a. The analysis was performed for 120 min of the photocatalytic reaction. Fig. 7b was used to calculate the kinetic parameters for the discoloration of RhB, as shown in Table 3. As shown in Fig. 7 and Table 3, CaO had a photocatalytic effect for the dye discoloration; i.e., its effect was dependent on the electromagnetic radiation. However, the material exhibited insulating behavior, as indicated by diffuse-reflectance analysis. When a UV lamp was used for photo-discoloration, the light energy (254 nm) was unable to excite the electrons of the VB to the CB of the material insulator.

To explain the photochemistry of RhB discoloration using CaO particles, it is proposed that electrons be transferred from the dye that

Table 2
Bandgap (eV) energy obtained from the UV/vis/NIR spectrum with the diffuse-reflectance modulus for the $SrTiO_3$, CaO, and CaO/$SrTiO_3$ heterostructure samples.

Sample	Band gap (eV)
$SrTiO_3$ (Pechini)	3.18
CaO (Pechini)	–
Ca + 0.5%STO	3.08 e 3.73
Ca + 1%STO	3.04 e 3.38
Ca + 2%STO	3.21
Ca + 5%STO	3.18
Ca + 10%STO	3.18

acts as an electrons donor -undergoing oxidation and initiating the discoloration process - by injecting electrons into the CaO CB rich in Ca $(OH)_2$ [1,33]. The injected electrons interacts with the O absorbed on the surface of the catalyst, producing superoxide radicals (O_2^{*-}) [1], which are among the most active species in the discoloration of RhB [20]. The following reactions are proposed.

$$RhB + h\nu \rightarrow RhB^* + e^- \quad (5)$$

$$CaO / Ca(OH)_2 + e^- \rightarrow CaO / Ca(OH)_2 (e^-_{CB}) \quad (6)$$

$$CaO / Ca(OH)_2 (e^-_{CB}) + O_2 \rightarrow CaO / Ca(OH)_2 + O_2^{*-} \quad (7)$$

$$O_2^{*-} + RhB \rightarrow RhB \text{ discoloration} \quad (8)$$

The heterostructures act as semiconductors, generating electrons and holes that are photogenerated by UV light. Thus, when an energy greater than or equal to the bandgap energy is provided, the CaO/$SrTiO_3$ heterojunction generates an exciton. The photogenerated electron can be captured by an O_2 molecule, forming a superoxide radical (O_2^{*-}). The holes can capture an electrons from the water or hydroxyl ions adsorbed on its surface, generating hydroxyl radicals (OH^*) that remain adsorbed on the surface of the catalyst [34]. The generated radicals and the electronic holes are responsible for oxidation reactions that discolor RhB. The following reactions are proposed for the heterojunctions.

$$CaO / SrTiO_3 + h\nu \rightarrow CaO / SrTiO_3 (e^-_{CB} + h^+_{VB}) \quad (9)$$

$$CaO / SrTiO_3 (e^-_{CB}) + O_2 \rightarrow CaO / SrTiO_3 + O_2^{*-} \quad (10)$$

$$CaO / SrTiO_3 (h^+_{VB}) + H_2O_{ads} \rightarrow CaO / SrTiO_3 + H^+ + OH^*_{ads} \quad (11)$$

$$CaO / SrTiO_3 (h^+_{VB}) + OH^-_{ads} \rightarrow CaO / SrTiO_3 + OH^*_{ads} \quad (12)$$

$$CaO / SrTiO_3 (h^+_{VB}) + RhB \rightarrow RhB^* + RhB \text{ oxidation} \quad (13)$$

$$OH^*_{ads} + RhB \rightarrow RhB \text{ discoloration} \quad (14)$$

$$O_2^{*-} + RhB \rightarrow RhB \text{ discoloration} \quad (15)$$

$$e^-_{CB} + h^+_{VB} \rightarrow \text{heat} \quad (16)$$

The lower PL intensities observed in the heterojunctions compared with pure CaO indicate that the recombination of electron/hole pairs occurred slowly, resulting in charge carriers acting at the surface of the material. In the case of the more photoactive heterojunction Ca + 2% STO, in addition to the doubly ionized vacancies ($[CaO_5.V_o^{\bullet\bullet}]$) detected by the photoluminescence emission in the green region, there were monoionized vacancies ($[CaO_5.V_o^{\bullet}]$) detected by the PL emission in the blue region, which acted both as electron donors and electron acceptors. In contrast, the heterostructures with less photocatalytic action did not exhibit active emission in the blue region, an emission increase in the green and red regions (indicating the presence of doubly ionized O vacancies ($[CaO_5.V_o^{\bullet\bullet}]$) that acted only as electron receptors), or an emission increase in the near-infrared region (indicating that the defects at the interface of the materials generated a more compact structure that reduced the photoactivity).

In the Kröger-Vink notation (Equations(17)–(20)), the subscripts *o* and *d* indicate ordered and disordered clusters, respectively. V_o^x and $V_o^{\bullet}$ indicate vacancies of neutral and monoionized O, respectively, and the superscript ' indicates an electron. All the CaO/$SrTiO_3$ heterostructures exhibited doubly ionized O vacancies ($V_o^{\bullet\bullet}$), and the heterostructures with $SrTiO_3$ concentrations of ≥2% also exhibited monoionized vacancies ($V_o^{\bullet}$).

$$[CaO_6]^x_o + [CaO_5.\ V^x_o]_d \rightarrow [CaO_6]'_o + [CaO_5.V^{\bullet}_o]_d \quad (17)$$

$$[CaO_5.V^{\bullet}_o]_d + [CaO_6]^x_o \rightarrow [CaO_5.V^{\bullet\bullet}_o]_d + [CaO_6]'_o \quad (18)$$

$$[SrO_{12}]^x_o + [SrO_{11}.V^x_o]_d \rightarrow [SrO_{12}]'_o + [SrO_{11}.\ V^{\bullet}_o]_d \quad (19)$$

$$[SrO_{12}]^x_o + [SrO_{11}.V^{\bullet}_o]_d \rightarrow [SrO_{12}]'_o + [SrO_{11}.\ V^{\bullet\bullet}_o]_d \quad (20)$$

The heterojunction with 2% $SrTiO_3$ exhibited the best photocatalytic performance owing to the monoionized O vacancy defects. The monoionized O vacancy defects increased the recombination time of the load carriers in relation to the others defects, such as doubly ionized O vacancies ($V_o^{\bullet\bullet}$), enhancing the photocatalytic activity. The role of the monoionized O vacancies in the photodegradation reactions was expected: these defects acted as donors (generating doubly ionized vacancies) and receptors of electrons (generating neutral vacancies), in contrast to doubly ionized vacancies, which only accepted electrons. Thus, the monoionized O vacancies acted as electronic bridges for charge-carrier transport.

4. Conclusion

CaO/$SrTiO_3$ heterojunctions were prepared via a sol-gel route. The

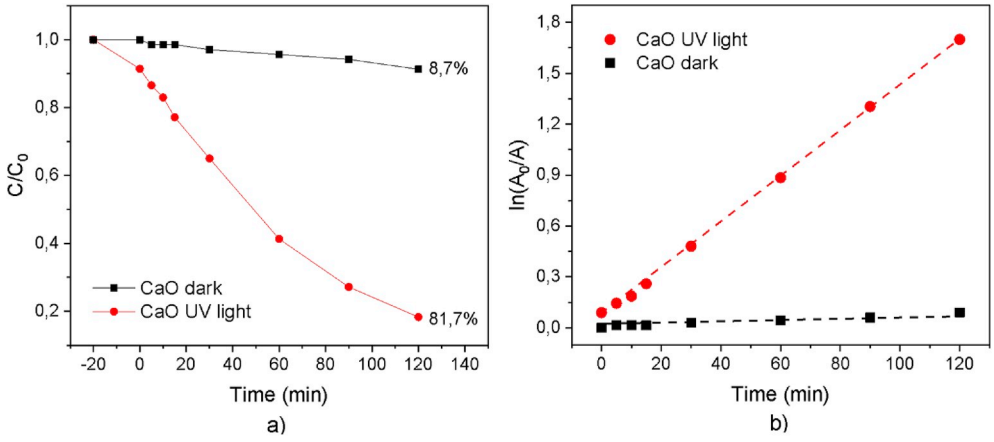

Fig. 7. a) Photocatalytic activity of CaO in the discoloration of RhB under UV light and in the dark; **b)** ln (A_0/A_t) versus time for discoloration.

Table 3
Kinetic parameters of RhB discoloration using CaO as a photocatalyst under light and in the dark.

Sample	Discoloration (120 min) (%)	k_{app} x 10^{-2} (min^{-1})	$t_{1/2}$ – calculated (min)	$t_{1/2}$ - observed (min)
CaO UV light	81.7	1.356	51.1	48.8
CaO dark	8.7	0.06704	1034.0	–

heterostructures were more photoactive than their precursors, i.e., pure CaO and $SrTiO_3$, owing to the formation of structural defects, such as O vacancies, which were good charge-trapping agents, increasing the recombination time of the excitons. The heterostructure with the highest photocatalytic activity (Ca + 2%STO) was the one with the greatest photoluminescent emission in the blue region, indicating that mono-ionized O vacancies were the most significant defects for increasing the photoactivity. Increasing the $SrTiO_3$ concentration beyond > 2% increased the interfacial defects and decreased the O vacancies, reducing the photoactivity. Decreasing the $SrTiO_3$ concentration below 2% decreased the amount of defects generated, causing a direct transition from the CB to the VB, reducing the photoactivity.

Acknowledgments

This work was supported by the São Paulo Research Foundation (Grant CEPID/CDMF - FAPESP: 2013/07296-2 and 2017/19143-7) and the National Council for Scientific and Technological Development (CNPq).

References

[1] M. Sanchez-Cantu, M.D.R. Peralta, A.B. Galindo-Rodriguez, E. Puente-Lopez, E. Rubio-Rosas, C.M. Gomez, F. Tzompantzi, Calcium-containing materials as alternative catalysts in advanced oxidation process, Fuel 198 (2017) 76–81, https://doi.org/10.1016/j.fuel.2016.11.092.
[2] J. Osuntokun, D.C. Onwudiwe, E.E. Ebenso, Aqueous extract of broccoli mediated synthesis of CaO nanoparticles and its application in the photocatalytic degradation of bromocrescol green, IET Nanobiotechnol. 12 (7) (2018) 888–894, https://doi.org/10.1049/iet-nbt.2017.0277.
[3] M.D.R. Peralta, M. Sanchez-Cantu, E. Puente-Lopez, E. Rubio-Rosas, F. Tzompantzi, Evaluation of calcium oxide in Rhodamine 6G photodegradation, Catal. Today 305 (2018) 75–81, https://doi.org/10.1016/j.cattod.2017.09.057.
[4] S.J. Abbas, P. Ramacharyulu, H.H. Lo, S.I. Ali, S.C. Ke, A catalytic approach to synthesis of PLP analogs and other environmental protocols in a single handed CaO/TiO_2 green nanoparticle, Appl. Catal. B Environ. 210 (2017) 276–289, https://doi.org/10.1016/j.apcatb.2017.03.075.
[5] P. Raizada, B. Priya, P. Thakur, P. Singh, Solar light induced photodegradation of oxytetracyline using Zr doped TiO_2/CaO based nanocomposite, Indian J. Chem. A. 55 (7) (2016) 803–809.
[6] T. Furusawa, M. Watanabe, R. Kadota, T. Matsumoto, M. Sato, N. Suzuki, Methanolysis of rapeseed oil to fatty acid methyl esters using microencapsulated CaO and TiO_2-supported chromium oxide under light irradiation, Fuel Process. Technol. 140 (2015) 125–131, https://doi.org/10.1016/j.fuproc.2015.09.003.
[7] M. Mohamad, N. Ngadi, S.L. Wong, M. Jusoh, N.Y. Yahya, Prediction of biodiesel yield during transesterification process using response surface methodology, Fuel 190 (2017) 104–112, https://doi.org/10.1016/j.fuel.2016.10.123.
[8] Y. Shaveisi, S. Sharifnia, Deriving Ag_3PO_4-CaO composite as a stable and solar light photocatalyst for efficient ammonia degradation from wastewater, J. Energy Chem. 27 (1) (2018) 290–299, https://doi.org/10.1016/j.jechem.2017.06.012.
[9] S. Zeng, P. Kar, U.K. Thakur, K. Shankar, A review on photocatalytic CO_2 reduction using perovskite oxide nanomaterials, Nanotechnology 29 (5) (2018), https://doi.org/10.1088/1361-6528/aa9fb1.
[10] W. Zhao, N.Q. Liu, H.X. Wang, L.H. Mao, Sacrificial template synthesis of core-shell $SrTiO_3/TiO_2$ heterostructured microspheres photocatalyst, Ceram. Int. 43 (6) (2017) 4807–4813, https://doi.org/10.1016/j.ceramint.2016.12.009.
[11] E. Drozdz, A. Kolezynski, The structure, electrical properties and chemical stability of porous Nb-doped $SrTiO_3$ - experimental and theoretical studies, RSC Adv. 7 (46) (2017) 28898–28908, https://doi.org/10.1039/c7ra04205a.
[12] C. Luo, J. Zhao, Y.X. Li, W. Zhao, Y.B. Zeng, C.Y. Wang, Photocatalytic CO_2 reduction over $SrTiO_3$: correlation between surface structure and activity, Appl. Surf. Sci. 447 (2018) 627–635, https://doi.org/10.1016/j.apsusc.2018.04.049.
[13] R.D. Kumar, R. Thangappan, R. Jayavel, Synthesis and characterization of $LaFeO_3/TiO_2$ nanocomposites for visible light photocatalytic activity, J. Phys. Chem. Solids 101 (2017) 25–33, https://doi.org/10.1016/j.jpcs.2016.10.005.
[14] C. Han, Q. Shao, J. Lei, Y.F. Zhu, S.S. Ge, Preparation of NiO/TiO_2 p-n heterojunction composites and its photocathodic protection properties for 304 stainless steel under simulated solar light, J. Alloy. Comp. 703 (2017) 530–537, https://doi.org/10.1016/j.jallcom.2017.01.349.
[15] K.K. Paul, N. Sreekanth, R.K. Biroju, T.N. Narayanan, P.K. Giri, Solar light driven photoelectrocatalytic hydrogen evolution and dye degradation by metal-free few-layer MoS_2 nanoflower/TiO_2(B) nanobelts heterostructure, Sol. Energy Mater. Sol. Cell. 185 (2018) 364–374, https://doi.org/10.1016/j.solmat.2018.05.056.
[16] R.A.C. Amoresi, V. Teodoro, G.F. Teixeira, M.S. Li, A.Z. Simoes, L.A. Perazolli, E. Longo, M.A. Zaghete, Electrosteric colloidal stabilization for obtaining $SrTiO_3/TiO_2$ heterojunction: microstructural evolution in the interface and photonics properties, J. Eur. Ceram. Soc. 38 (4) (2018) 1621–1631, https://doi.org/10.1016/j.jeurceramsoc.2017.10.056.
[17] J. Ng, S.P. Xu, X.W. Zhang, H.Y. Yang, D.D. Sun, Hybridized nanowires and cubes: a novel architecture of a heterojunctioned $TiO_2/SrTiO_3$ thin film for efficient water splitting, Adv. Funct. Mater. 20 (24) (2010) 4287–4294, https://doi.org/10.1002/adfm.201000931.
[18] J. Zhang, J.H. Bang, C.C. Tang, P.V. Kamat, Tailored TiO_2-$SrTiO_3$ heterostructure nanotube Arrays for improved photoelectrochemical performance, ACS Nano 4 (1) (2010) 387–395, https://doi.org/10.1021/nn901087c.
[19] A. Fujishima, X.T. Zhang, D.A. Tryk, TiO_2 photocatalysis and related surface phenomena, Surf. Sci. Rep. 63 (12) (2008) 515–582, https://doi.org/10.1016/j.surfrep.2008.10.001.
[20] U. Coleto, R.A.C. Amoresi, V. Teodoro, I.M. Iani, E. Longo, M.A. Zaghete, L.A. Perazolli, An approach for photodegradation mechanism at $TiO_2/SrTiO_3$ interface, J. Mater. Sci. Mater. Electron. 29 (23) (2018) 20329–20338, https://doi.org/10.1007/s10854-018-0167-x.
[21] J.X. Yu, Z.G. Chen, L. Zeng, Y.Y. Ma, Z. Feng, Y. Wu, H.J. Lin, L.H. Zhao, Y.M. He, Synthesis of carbon-doped $KNbO_3$ photocatalyst with excellent performance for photocatalytic hydrogen production, Sol. Energy Mater. Sol. Cell. 179 (2018) 45–56, https://doi.org/10.1016/j.solmat.2018.01.043.
[22] A. Golubovic, M. Scepanovic, A. Kremenovic, S. Askrabic, V. Berec, Z. Dohcevic-Mitrovic, Z.V. Popovic, Raman study of the variation in anatase structure of TiO_2 nanopowders due to the changes of sol-gel synthesis conditions, J. Sol. Gel Sci. Technol. 49 (3) (2009) 311–319, https://doi.org/10.1007/s10971-008-1872-3.
[23] I.H. Campbell, P.M. Fauchet, The effects of microcrystal size and shape on the one phonon Raman-spectra of crystalline semiconductors, Solid State Commun. 58 (10) (1986) 739–741, https://doi.org/10.1016/0038-1098(86)90513-2.
[24] F. Cerdeira, Cj Buchenau, F.H. Pollak, M. Cardona, Stress induced shifts of first order Raman frequencies of zincblende-and diamond-type semiconductors, Bull. Am. Phys. Soc. 16 (1) (1971) 29–&, https://doi.org/10.1103/PhysRevB.5.580.
[25] M.J. Scepanovic, M.U. Grujic-Brojcin, Z.D. Dohcevic-Mitrovic, Z.V. Popovic, Effects of confinement, strain and nonstoichiometry on Raman spectra of anatase TiO_2 nanopowders, Mater. Sci. Forum 518 (2006) 101–106 https://doi.org/10.4028/www.scientific.net/MSF.518.101.
[26] O. Frank, G. Tsoukleri, J. Parthenios, K. Papagelis, I. Riaz, R. Jalil, K.S. Novoselov, M. Kalbac, L. Kavan, C. Galiotis, T. Ltd, Graphene under uniaxial deformation: a Raman study, Nanocontainers 2011 (2011) 225–230.
[27] Y. Lei, L.D. Zhang, G.W. Meng, G.H. Li, X.Y. Zhang, C.H. Liang, W. Chen, S.X. Wang, Preparation and photoluminescence of highly ordered TiO_2 nanowire arrays, Appl. Phys. Lett. 78 (8) (2001) 1125–1127, https://doi.org/10.1063/1.1350959.
[28] J.C. Yu, J.G. Yu, W.K. Ho, Z.T. Jiang, L.Z. Zhang, Effects of F- doping on the photocatalytic activity and microstructures of nanocrystalline TiO_2 powders, Chem. Mater. 14 (9) (2002) 3808–3816, https://doi.org/10.1021/cm020027c.
[29] J.W. Liu, J. Li, A. Sedhain, J.Y. Lin, H.X. Jiang, Structure and photoluminescence study of TiO_2 nanoneedle texture along vertically aligned carbon nanofiber arrays, J. Phys. Chem. C 112 (44) (2008) 17127–17132, https://doi.org/10.1021/jp8060653.
[30] J.M. Wu, H.C. Shih, W.T. Wu, Y.K. Tseng, I.C. Chen, Thermal evaporation growth and the luminescence property of TiO_2 nanowires, J. Cryst. Growth 281 (2–4) (2005) 384–390, https://doi.org/10.1016/j.jcrysgro.2005.04.018.
[31] V.M. Longo, A.T. de Figueiredo, S. de Lazaro, M.F. Gurgel, M.G.S. Costa, C.O. Paiva-Santos, J.A. Varela, E. Longo, V.R. Mastelaro, F.S. De Vicente, A.C. Hernandes, R.W.A. Franco, Structural conditions that leads to photoluminescence emission in $SrTiO_3$: an experimental and theoretical approach, J. Appl. Phys. 104 (2) (2008), https://doi.org/10.1063/1.2956741.
[32] Y.J. Zhang, J. Wang, M.P.K. Sahoo, T. Shimada, T. Kitamura, Mechanical control of magnetism in oxygen deficient perovskite $SrTiO_3$, Phys. Chem. Chem. Phys. 17 (40) (2015) 27136–27144, https://doi.org/10.1039/c5cp04310g.
[33] F. Chen, W.W. Zou, W.W. Qu, J.L. Zhang, Photocatalytic performance of a visible light TiO_2 photocatalyst prepared by a surface chemical modification process, Catal. Commun. 10 (11) (2009) 1510–1513, https://doi.org/10.1016/j.catcom.2009.04.005.
[34] D. Adak, S. Ghosh, P. Chakraborty, K.M.K. Srivatsa, A. Mondal, H. Saha, R. Mukherjee, R. Bhattacharyya, Non lithographic block copolymer directed self-assembled and plasma treated self-cleaning transparent coating for photovoltaic modules and other solar energy devices, Sol. Energy Mater. Sol. Cell. 188 (2018) 127–139, https://doi.org/10.1016/j.solmat.2018.08.011.